Front. Phys. 13(3), 138110 (2018)
https://doi.org/10.1007/s11467-018-0753-7

RESEARCH ARTICLE

Ultrathin nanosheets of Mn_3O_4: A new two-dimensional ferromagnetic material with strong magnetocrystalline anisotropy

Jun-Chi Wu[1,#], Xu Peng[1,#], Yu-Qiao Guo[1], Hao-Dong Zhou[1], Ji-Yin Zhao[1], Ke-Qin Ruan[1], Wang-Sheng Chu[2], Changzheng Wu[1,†]

[1] *Hefei National Laboratory for Physical Sciences at the Microscale, iChEM (Collaborative Innovation Center of Chemistry for Energy Materials), CAS Center for Excellence in Nanoscience, and CAS Key Laboratory of Mechanical Behavior and Design of Materials, University of Science and Technology of China, Hefei 230026, China*
[2] *National Synchrotron Radiation Laboratory, University of Science and Technology of China, Hefei 230026, China*
Corresponding author. E-mail: †czwu@ustc.edu.cn
Received January 24, 2018; accepted March 20, 2018

Two-dimensional (2D) materials with robust ferromagnetism have played a key role in realizing next-generation spin-electronic devices, but many challenges remain, especially the lack of intrinsic ferromagnetic behavior in almost all 2D materials. Here, we highlight ultrathin Mn_3O_4 nanosheets as a new 2D ferromagnetic material with strong magnetocrystalline anisotropy. Magnetic measurements along the in-plane and out-of-plane directions confirm that the out-of-plane direction is the easy axis. The 2D-confined environment and Rashba-type spin-orbit coupling are thought to be responsible for the magnetocrystalline anisotropy. The robust ferromagnetism in 2D Mn_3O_4 nanosheets with magnetocrystalline anisotropy not only paves a new way for realizing the intrinsic ferromagnetic behavior in 2D materials but also provides a novel candidate for building next-generation spin-electronic devices.

Keywords 2D ferromagnetic material, topochemical conversion, magnetocrystalline anisotropy

PACS numbers 75.70.Ak, 81.10.St, 75.30.Gw

1 Introduction

Since the discovery of graphene, the family of two-dimensional (2D) materials has greatly expanded, exhibiting a broad range of novel physics properties and potential applications. High carrier mobility and on/off ratio have been realized in graphene and transition-metal chalcogenide (TMC)-based field-effect transistors, making them a bright prospect for next-generation flexible devices [1–3]. Even so, the lack of long-range ferromagnetic order because of the strong thermal fluctuations in the 2D flat plane according to the Mermin–Wagner theorem hinders long-range spin ordering, impeding their further application in spin-electronic devices [4]. Various methods, including surface modification, defect engineering, and doping with magnetic atoms were adopted as attempts to induce ordered magnetism in 2D materials [5–8]. However, with these approaches, it is difficult to introduce long-range correlations between exotic local magnetic moments by solid exchange interactions. Recently, 2D CrI_3 and $CrGeTe_3$ nanosheets were found to be ferromagnetic within a 2D limit [9, 10]. Magnetic anisotropy was highlighted as a factor crucial for realizing 2D ferromagnetism, thereby guiding the search for more 2D magnetic materials [11]. However, the 2D iodide and telluride nanosheets suffered from poor stability even in the bulk form, hampering their development in practical devices. Therefore, stable ferromagnetism in 2D materials is highly desirable and leaves plenty of room for further exploring new magnetic material systems.

Spinel structural transition metal oxides (TMOs) are a series of classical soft ferromagnets with excellent thermodynamic stability, and most of them exhibit strong magnetocrystalline anisotropy due to the intercoupling among the electronic orbits, crystal fields, and spins [12–14]. Space confinement in one crystal orientation with a special spin orientation is expected to result in 2D ferromagnetism in the spinel TMOs. Unfortunately, it is difficult to obtain ultrathin freestanding nanosheets with

*Special Topic: Inorganic Two-Dimensional Nanomaterials (Eds. Changzheng Wu & Xiaojun Wu). #These authors contributed equally to this work.

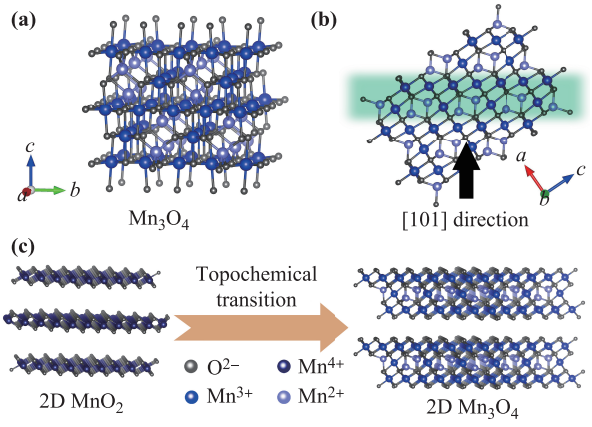

Fig. 1 **(a)** Crystal structure of bulk Mn_3O_4. **(b)** Side-view of Mn_3O_4 along b axis. **(c)** Schematic diagram of topochemical conversion from 2D MnO_2 nanosheets to 2D Mn_3O_4 nanosheets.

traditional top-down methods because the bulk spinel structure crystallizes into a highly solid 3D chemical bonding network. Herein, we developed a topochemical conversion strategy for the synthesis of 2D spinel Mn_3O_4 nanosheets with strong magnetic anisotropy and intrinsic long-range ferromagnetic order. The crystal structure of Mn_3O_4 is shown in Fig. 1(a). Notably, Mn_3O_4 contains two types of Mn-O layers in the (101) crystalline facet. One contains the MnO_6 octahedrons and the other contains both MnO_6 octahedrons and MnO_4 tetrahedrons. As shown in Fig. A1, the former is highly similar to a single δ-MnO_2 layer formed by all the MnO_6 octahedrons, and the latter could form by a partial distortion of the MnO_2 layer structure [15]. During a low-oxygen-pressure thermo-annealing process, the δ-MnO_2 nanosheets could transform to Mn_3O_4 nanosheets by forming disordered layers sandwiched between the unchanging MnO_2 layers, as shown in Fig. 1(b). The topochemical conversion process to layered Mn_3O_4 from layered δ-MnO_2 is shown in Fig. 1(c). It is notable that by the topochemical conversion process, the crystalline facet of the freestanding Mn_3O_4 nanosheets can be spontaneously controlled to be (101), which is helpful for the research on magnetocrystalline anisotropy.

2 Experiments and analysis

The Mn_3O_4 nanosheets were achieved by topological conversion through the low-oxygen pressure thermo-annealing of the δ-MnO_2 nanosheets at 300°C. The experimental details are given in Supplemental Materials. The phases of the as-obtained product and purchased Mn_3O_4 powder were confirmed by X-ray diffraction (XRD) analysis. As shown in Fig. 2(a), the XRD pattern

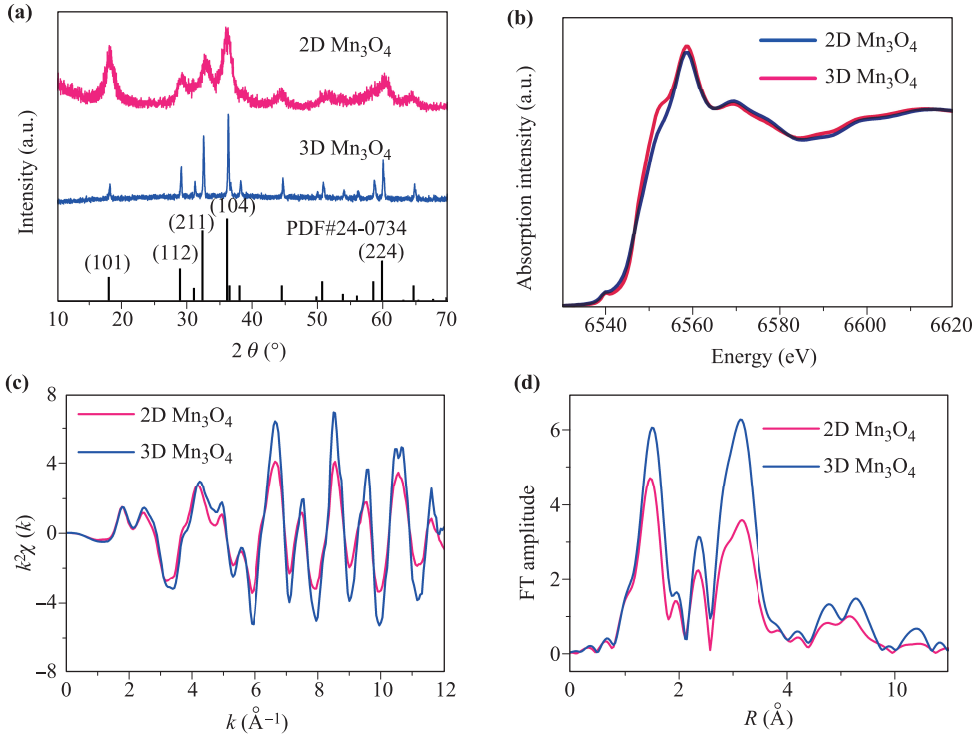

Fig. 2 **(a)** XRD patterns of the 2D Mn_3O_4 nanosheets and 3D Mn_3O_4 powder. Mn K-edge **(b)** XANES spectra, **(c)** EXAFS oscillation function $k^2\chi(k)$ and **(d)** the corresponding Fourier transformations FT($k^2\chi(k)$) for 2D Mn_3O_4 nanosheets and 3D Mn_3O_4 powder.

of the as-obtained sample can be indexed to hausmannite Mn_3O_4 (space group l41, JCPDS card No. 24-0734), indicating that the as-obtained Mn_3O_4 nanosheets are successfully transformed by the δ-MnO_2 nanosheets. Possible impurities (e.g., MnO_2, MnO, and Mn_2O_3) were excluded by carefully contrasting the XRD results with the standard patterns that include those of Mn_3O_4, MnO_2, MnO, and Mn_2O_3, as shown in Fig. A2. Compared to the 3D Mn_3O_4 powder, 2D Mn_3O_4 nanosheets present broadened diffraction peaks without any obvious peak shifts. The same diffraction peaks imply the 2D Mn_3O_4 retains the same lattice symmetry or long-range structure of 3D Mn_3O_4. The increased full width at half maximum (FWHM) suggests the short-range local distortion exits and reduces the crystallinity. The remarkably enhanced intensity of the (101) peak suggests [101] to be the preferential orientation, agreeing with our topochemical design. X-ray absorption fine structure (XAFS), which is usually used for detecting the electronic structure and fine local atomic structure, was utilized to explore the local structure around the Mn atoms. A standard pure Mn_3O_4 powder was used as a comparison. The XAFS data were carefully normalized for semi-quantitative analysis. The white line peak experiences a distinct red shift in 2D Mn_3O_4, verifying a reduced chemical valence due to the 2D confined environment, as shown in Fig. 2(b). The similar radial pair distribution functions, with decreased amplitudes in the k space, suggest no large Mn_3O_4 lattice framework change, but a decreased coordination number around the Mn atoms in the 2D nanosheets, as shown in Fig. 2(c). The differences in the coordination environment became clear after the Fourier transform of the k space into the R space. As shown in Fig. 2(d), all the peaks of 3D Mn_3O_4 remain in 2D Mn_3O_4, suggesting the form of coordination does not change with dimensional reduction. The peaks at 1.53 Å and 2.36 Å correspond to two types of Mn-O shell shift to 1.48 Å and 2.35 Å, implying a shortened Mn-O distance in the 2D Mn_3O_4 nanosheets because of dimensional confinement. In addition, the peak at 3.13 Å corresponds to the Mn-Mn shell, the amplitudes of which for 2D and 3D Mn_3O_4 are about 3.54 and 6.26, respectively. The intensity of the Mn-Mn shell decreases by 43% compared with 3D Mn_3O_4, which is consistent with the decreased coordination number and structural distortion of the 2D Mn_3O_4 lattice. The deficiency in coordination structure and atomic distortion has also been found in other classical 2D oxide nanosheets with non-layered crystal structures and revealed novel chemical and physical properties [16–18].

To verify the 2D morphology of Mn_3O_4 nanosheets after topological conversion, a series of microscopic characterizations were carried out. The field-emission scanning electron microscopy (FE-SEM) image presented in

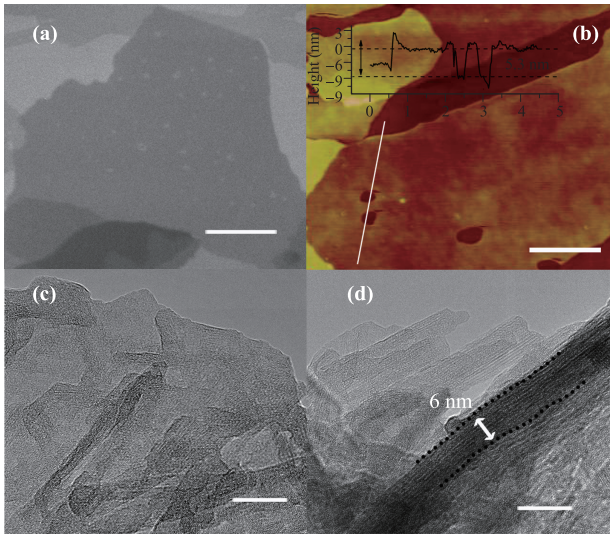

Fig. 3 **(a)** SEM image of the Mn_3O_4 nanosheets, scale bar: 1 μm. **(b)** AFM image of Mn_3O_4 nanosheets, scale bar: 2 μm. **(c)** HRTEM image of the Mn_3O_4 nanosheets, scale bar: 10 nm. **(d)** Edge-area HRTEM image of Mn_3O_4 nanosheets, scale bar: 10 nm.

Fig. 3(a) clearly shows the 2D morphology of Mn_3O_4 nanomaterial with sporadic nanoholes after thermo-annealing at 300°C. At a higher annealing temperature, the 2D morphology starts to become broken with visible aggregation, as shown in the SEM image in Fig. A3. Moreover, the height of a single nanosheet was evaluated to be approximately 5.3 nm by the atomic force microscopy (AFM) image in Fig. 3(b). In the HRTEM image in Fig. 3(c), the contrast of nanosheets suggests an ultrathin 2D situation of Mn_3O_4 nanosheets. Furthermore, the edge-area HRTEM image in Fig. 3(d) shows the 6-nm thickness of a nanosheet, further confirming the nanometer-size thickness of 2D Mn_3O_4 sheets. These experimental results clearly confirm the thermo-annealing product of 2D MnO_2 nanosheets to be 2D Mn_3O_4 nanosheets with ultrathin thickness.

In order to investigate the intrinsic magnetism of the 2D Mn_3O_4 nanosheets, especially the magnetocrystalline anisotropy, the detailed magnetic properties were recorded using a vibrating sample magnetometer-superconducting quantum interference device (VSM-SQUID). By a vacuum filtration process, a compact Mn_3O_4 film with consistent crystalline facets was self-assembled and stacked with a consistent crystal orientation of [101]. The magnetic hysteresis loops measured at 10 K with the magnetic field parallel (in-plane magnetic field) and perpendicular to the film (out-of-plane magnetic field) are shown in Fig. 4(a). The results exhibit two completely different hysteresis behaviors for the in-plane and out-of-plane magnetic fields. In detail, the curve measured in the out-of-plane direction shows

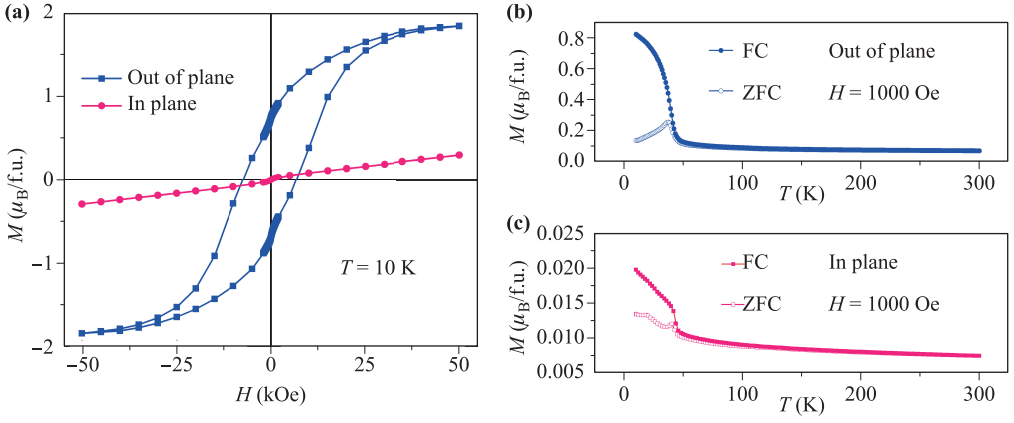

Fig. 4 **(a)** M-H curves for 2D Mn_3O_4 measured at 10 K with anisotropy behavior. Temperature dependence of ZFC and FC magnetization of 2D Mn_3O_4 in **(b)** out-of-plane and **(c)** in-plane magnetic field.

a distinct looped behavior with large saturation magnetization, whereas the magnetic susceptibility measured in the in-plane magnetic field exhibits an almost linear function of an exotic magnetic field, except for a slight magnetization behavior in the small field. In addition, the coercivity and remnant magnetization in the out-of-plane magnetic field direction are much larger than that in the in-plane magnetic field direction, demonstrating robust anisotropic ferromagnetism. The larger saturation magnetization, coercivity, and remnant magnetization suggest the out-of-plane direction to be the easy-axis direction.

To further comprehend the magnetic properties of 2D Mn_3O_4, the temperature dependence of magnetization was measured from 10 K to 300 K in a magnetic field of 1000 Oe along the in-plane and out-of-plane directions. As shown in Fig. 4(b), when the magnetic field is controlled along the out-of-plane direction, the zero-field-cooling (ZFC) curve increases gradually at low temperatures until it reaches a maximum at approximately 39 K, before decreasing continually. Meanwhile, the field-cooling (FC) curve decreases within the whole temperature region, and at approximately 45 K, the FC curve merges with the ZFC curve. The results prove that a transition from the paramagnetic phase to the ferrimagnetic phase with a triangular spin arrangement occurs in 2D Mn_3O_4. Similarly, the magnetic phase transition also emerges in an in-plane magnetic field at 39 K. However, the magnetization is quite weak, less than one-tenth of magnetization in an out-of-plane magnetic field of 1000 Oe.

These experimental results strongly confirm the magnetocrystalline anisotropy of 2D Mn_3O_4, with the easy axis along the [101] direction. However, it has been reported that in 3D Mn_3O_4 single crystals or 2D Mn_3O_4 thin films, the [100] direction is the easy axis and the [001] direction is the hard axis [19, 20]. The abnormal easy axis tilt when the dimensionality of Mn_3O_4 is reduced to the 2D limit is extraordinary. Fundamentally, the magnetocrystalline anisotropy in bulk Mn_3O_4 originates from elongated Mn-O bonds in MnO_6 octahedrons along the [001] direction because of the Jahn–Teller effect on Mn^{3+} according to Vafet–Kittel theory [21]. Several studies on Mn_3O_4 films grown on special substrates found that the hard axis could soften and the soft axis could harden when the thickness decreased, suggesting that 2D confinement could influence magnetocrystalline anisotropy to some extent [22, 23]. It is notable that all previous studies focused on certain crystalline orientations, such as [100], [110], and [001], to match with the substrate. Here, our unique topochemical approach enables us to obtain freestanding Mn_3O_4 nanosheets with the [101] orientation. The long-range period along [100] or [001] would be destroyed and lead to a tilting of the easy axis away from the [100] direction, with a tilt angle of approximately 32°.

From the perspective of structure, the 2D Mn_3O_4 is stacked by two types of MnO_x layers along the [101] direction, which is inherited by 2D Mn_3O_4, as shown in Fig. A4. The alternatively stacked structure provides unique symmetry breaking in 2D Mn_3O_4. As shown in Fig. A5, the mirror symmetry does not exist along the [101] direction in 3D Mn_3O_4, and is absent in 2D Mn_3O_4 as well. Furthermore, the 2D Mn_3O_4 is not equal to its counterpart after an inversion operation, implying a space inversion asymmetry. The asymmetry environment will induce a Rashba type spin-orbit coupling and force the electronic spin point along the out-of-plane direction, then give rise to a strong 2D magnetic character [24, 25]. Therefore, the asymmetry environment in 2D Mn_3O_4 is considered the primary cause of easy axis tilting.

3 Conclusion

In summary, by a topochemical strategy, freestanding 2D Mn_3O_4 nanosheets with the [101] orientation were successfully synthesized and exhibited strong ferromagnetism with magnetocrystalline anisotropy. Robust ferromagnetism with large saturated magnetization, coercivity, and remnant magnetization was found in the direction of the magnetic field perpendicular to the film, but a weak ferromagnetism was observed in the field direction parallel to the film. An unexpected tilt of the easy axis was observed because of strong Rashba-type spin-orbit coupling. The 2D ferromagnetic Mn_3O_4 nanosheet provides a new candidate for flexible spin-electronic materials.

Acknowledgements This work was financially supported by the National Basic Research Program of China (Grant No. 2015CB932302), the Youth Innovation Promotion Association CAS, the National Natural Science Foundation of China (Grant Nos. 21501164, U1632154, and J1030412), National Young Top-Notch Talent Support Program, the Chinese Academy of Sciences (Grant No. XDB01020300), the Fok Ying-Tong Education Foundation, China (Grant No. 141042), the Anhui Provincial Natural Science Foundation (Grant No. 1608085QA08), and the Fundamental Research Funds for the Central Universities (Grant Nos. WK2060190027, WK2310000055, and WK2340000065). We would like to thank the staff at beamlines BL14W1 (Shanghai Synchrotron Radiation Facility) for providing beam time and for their helpful discussions.

Appendix A Supplementary information

A.1 Experimental section

Materials. Manganese chloride ($MnCl_24H_2O$), ammonium persulfate ($(NH_4)_2S_2O_8$), and tetramethylammonium hydroxide (TMAOH) were purchased from Sinopharm Chemical Reagent Co. Ltd. (Shanghai, China). All chemicals were used directly without further purification.

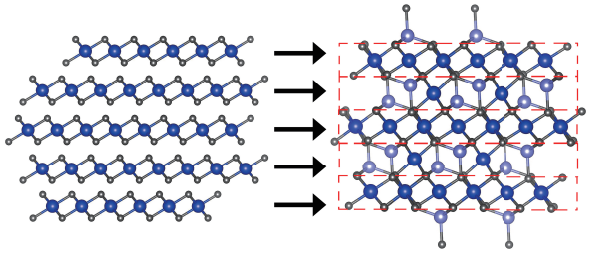

Fig. A1 Scheme of topochemical similarity between MnO_2 and Mn_3O_4.

Synthesis of δ-MnO_2. δ-MnO_2 was synthesized according to our previous work (Ref. [15]). In a typical experiment, 0.6 g $MnCl_24H_2O$ was dissolved in 10 mL H_2O, denoted as "solution A." Then, 4.0 g $(NH_4)_2S_2O_8$ and 4.375 g TMAOH (25% wt) were added to 10 mL H_2O in two steps, denoted as "solution B." Then "solution B" was dropwise added into "solution A" under vigorous stirring. The mixed solution was vigorously stirred overnight at room temperature to generate δ-MnO_2. The

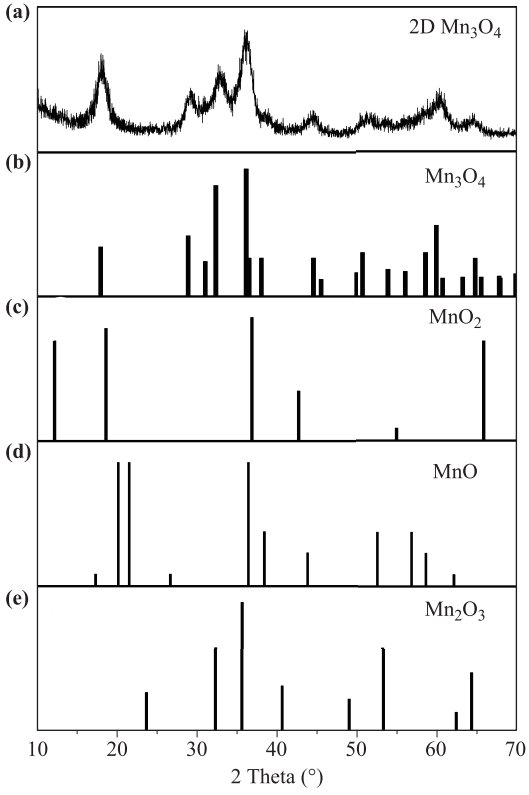

Fig. A2 **(a)** XRD pattern of 2D Mn_3O_4 and standard XRD patterns of **(b)** Mn_3O_4, **(c)** MnO_2, **(d)** MnO, and **(e)** Mn_2O_3.

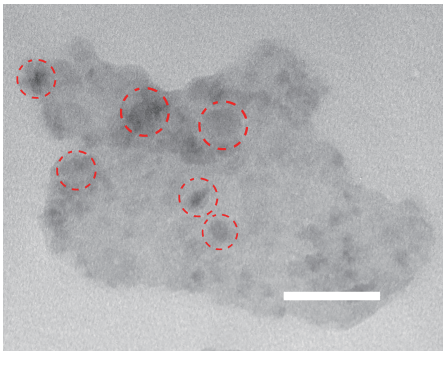

Fig. A3 SEM image of product under annealing temperature of 320°C, in which distinguished nanoparticles are emphasized by dotted red lines. Scale bar: 50 nm.

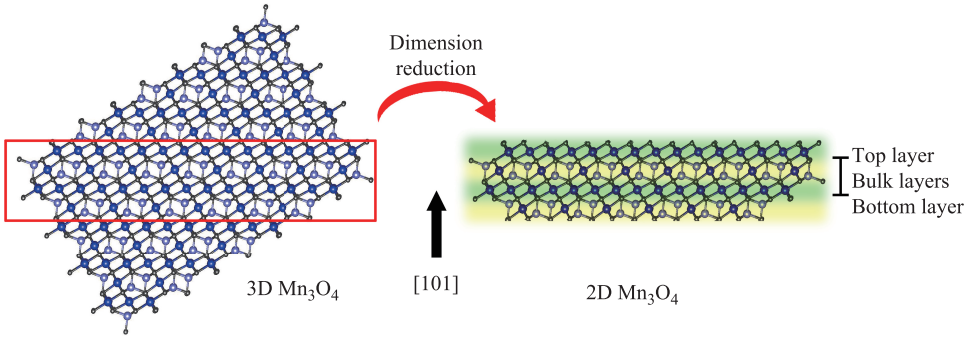

Fig. A4 Scheme of dimension reduction process of Mn_3O_4. The green and yellow stripes represent two types of MnO_x layers, respectively.

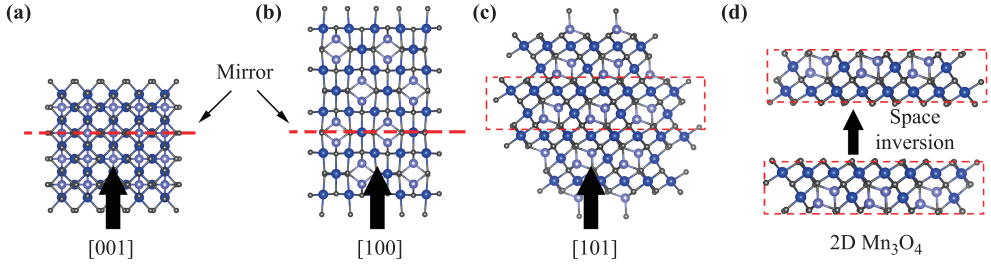

Fig. A5 Schemes of 3D Mn_3O_4 along **(a)** [001], **(b)** [100], and **(c)** [101] directions. **(d)** 2D Mn_3O_4 and its broken space inversion asymmetry.

product was collected by centrifugation and washed with methanol and water several times; then, the precipitate was dried in vacuum at 60°C.

Synthesis of 2D Mn_3O_4 by a topochemical approach. The δ-MnO_2 product was allowed to thermo-anneal at 300°C for 2 h in a N_2 atmosphere to obtain stacked Mn_3O_4. The stacked Mn_3O_4 was dispersed in water and sonicated for 1 h at room temperature to obtain 2D Mn_3O_4. The unexfoliated bulk Mn_3O_4 was separated as dispersions after centrifugation under a low rotation speed. The Mn_3O_4 nanosheets were collected by vacuum filtered over a cellulose membrane.

Characterization. X-ray diffraction (XRD) was measured using a Philips X' Pert Pro Super diffractometer with Cu Kα radiation ($\lambda = 1.54178$ Å) with a scanning speed of 8°/min. The field emission scanning electron microscopy images were obtained on a Zeiss Gemini300 scanning electron microscope. Atomic-force microscope (AFM) images were acquired by a Veeco DI Nano-scope Multi-Mode V system. High-resolution transmission electron microscopy images were performed in a JEOL-2010TEM with an acceleration voltage of 200 kV.

X-ray absorption spectroscopy (XAS) measurements. The X-ray absorption spectra at the Mn K-edge of the samples were collected at the beam line BL14W1 of the Shanghai Synchrotron Radiation Facility (SSRF, China) at room temperature in the transmission mode, operated with a Si(111) double crystal monochromator. The storage ring was operated at an energy of 3.5 GeV and a current between 150 and 210 mA during the measurement process. The photon energy was verified by calibrating the first inflection point of the Mn K-edge in a Mn metal foil. The X-ray absorption spectra (EXAFS) data were fitted in the R space using the IFEFFIT code [1], and the scattering amplitudes and the phase shifts were generated by the Feff8 code [2]. All FT curves of the 2D and 3D Mn_3O_4 nanosheets were reconstructed successfully with the X-ray crystalline data of the local structure of the octahedral site of Mn_3O_4 (Ia3) as the initial models.

Magnetic property measurements. A film constituted by freestanding Mn_3O_4 nanosheets by vacuum filter was prepared for the magnetic measurements. The magnetization was characterized using a SQUID (quantum design MPMS XL-7) magnetometer with temperature ranging from 10 to 300 K and the applied field varying between −50 and 50 kOe.

Supporting references

1. B. Ravel and M. Newville, ATHENA, ARTEMIS, HEPHAESTUS: Data analysis for X-ray absorption spectroscopy using IFEFFIT, *J. Synchrotron Radiat.* 12(4), 537 (2005)

2. A. Ankudinov, B. Ravel, J. Rehr, and S. Conradson, Real-space multiple-scattering calculation and interpretation of X-ray-absorption near-edge structure, *Phys. Rev. B* 58(12), 7565 (1998)

References

1. K. S. Novoselov, A. K. Geim, S. V. Morozov, D. Jiang, Y. Zhang, S. V. Dubonos, I. V. Grigorieva, and A. A. Firsov, Electric field effect in atomically thin carbon films, *Science* 306(5696), 666 (2004)
2. Q. H. Wang, K. Kalantarzadeh, A. Kis, J. N. Coleman, and M. S. Strano, Electronicsand optoelectronics of two-dimensional transition metal dichalcogenides, *Nat. Nanotechnol.* 7(11), 699 (2012)
3. P. Ajayan, P. Kim, and K. Banerjee, Two-dimensional van der Waals materials, *Phys. Today* 69(9), 38 (2016)
4. S. Rudin and D. C. Mattis, Absence of ferromagnetism in the two-dimensional Hubbard model, *Phys. Lett. A* 110(5), 273 (1985)
5. K. Xu, X. Li, P. Chen, D. Zhou, C. Wu, Y. Guo, L. Zhang, J. Zhao, X. Wu, and Y. Xie, Hydrogen dangling bonds induce ferromagnetism in two-dimensional metal-free graphitic-C_3N_4 nanosheets, *Chem. Sci.* 6(1), 283 (2015)
6. X. Zhu, Y. Guo, H. Cheng, J. Dai, X. An, J. Zhao, K. Tian, S. Wei, X. Cheng Zeng, C. Wu, and Y. Xie, Signature of coexistence of superconductivity and ferromagnetism in two-dimensional $NbSe_2$ triggered by surface molecular adsorption, *Nat. Commun.* 7, 11210 (2016)
7. L. Cai, J. He, Q. Liu, T. Yao, L. Chen, W. Yan, F. Hu, Y. Jiang, Y. Zhao, T. Hu, Z. Sun, and S. Wei, Vacancy-induced ferromagnetism of MoS_2 nanosheets, *J. Am. Chem. Soc.* 137(7), 2622 (2015)
8. B. Li, T. Xing, M. Zhong, L. Huang, N. Lei, J. Zhang, J. Li, and Z. Wei, A two-dimensional Fe-doped SnS_2 magnetic semiconductor, *Nat. Commun.* 8(1), 1958 (2017)
9. B. Huang, G. Clark, E. Navarro-Moratalla, D. R. Klein, R. Cheng, K. L. Seyler, D. Zhong, E. Schmidgall, M. A. Mcguire, D. H. Cobden, W. Yao, D. Xiao, P. Jarillo-Herrero, and X. Xu, Layer-dependent ferromagnetism in a van der Waals crystal down to the monolayer limit, *Nature* 546(7657), 270 (2017)
10. C. Gong, L. Li, Z. Li, H. Ji, A. Stern, Y. Xia, T. Cao, W. Bao, C. Wang, Y. Wang, Z. Q. Qiu, R. J. Cava, S. G. Louie, J. Xia, and X. Zhang, Discovery of intrinsic ferromagnetism in two-dimensional van der Waals crystals, *Nature* 546(7657), 265 (2017)
11. J. L. Miller, Ancient clues help quantify modern methane, *Phys. Today* 70, 16 (2017)
12. H. T. Jeng and G. Y. Guo, First-principles investigations of the electronic structure and magnetocrystalline anisotropy in strained magnetite Fe_3O_4, *Phys. Rev. B* 65(9), 094429 (2002)
13. K. Dwight and N. Menyuk, Magnetic properties of and the canted spin problem, *Phys. Rev.* 119(5), 1470 (1960)
14. T. Jeng and G. Y. Guo, First-principles investigations of the electronic structure and magnetocrystalline anisotropy in strained magnetite Fe_3O_4, *Phys. Rev. B* 65(9), 094429 (2002)
15. X. Peng, Y. Guo, Q. Yin, J. Wu, J. Zhao, C. Wang, S. Tao, W. Chu, C. Wu, and Y. Xie, Double-exchange effect in two-dimensional MnO_2 nanomaterials, *J. Am. Chem. Soc.* 139(14), 5242 (2017)
16. W. Cheng, J. He, T. Yao, Z. Sun, Y. Jiang, Q. Liu, S. Jiang, F. Hu, Z. Xie, B. He, W. Yan, and S. Wei, Half-unit-cell α-Fe_2O_3 semiconductor nanosheets with intrinsic and robust ferromagnetism, *J. Am. Chem. Soc.* 136(29), 10393 (2014)
17. Y. Sun, Q. Liu, S. Gao, H. Cheng, F. Lei, Z. Sun, Y. Jiang, H. Su, S. Wei, and Y. Xie, Pits confined in ultrathin cerium(IV) oxide for studying catalytic centers in carbon monoxide oxidation, *Nat. Commun.* 4, 2899 (2013)
18. L. Liang, J. Zhang, Y. Zhou, J. Xie, X. Zhang, M. Guan, B. Pan, and Y. Xie, High-performance flexible electrochromic device based on facile semiconductor-to-metal transition realized by $WO_3{\cdot}2H_2O$ ultrathin nanosheets, *Sci. Rep.* 3(1), 1936 (2013)
19. G. Srinivasan and M. S. Seehra, Magnetic properties of Mn_3O_4 and a solution of the canted-spin problem, *Phys. Rev. B* 28(1), 1 (1983)
20. L. Ren, S. Wu, M. Yang, W. Zhou, and S. Li, Magnetic properties of Mn_3O_4 film under compressive stress grown on $MgAl_2O_4$ (001) by molecular beam epitaxy, *J. Appl. Phys.* 114(5), 053907 (2013)
21. Y. Yafet and C. Kittel, Antiferromagnetic arrangements in ferrites, *Phys. Rev.* 87(2), 290 (1952)
22. L. Ren, M. Yang, W. Zhou, S. Wu, and S. Li, Influence of stress and defect on magnetic properties of Mn_3O_4 films grown on $MgAl_2O_4$ (001) by molecular beam epitaxy, *J. Phys. Chem. C* 118(1), 243 (2014)
23. L. Ren, W. Zhou, Y. Wang, M. Meng, S. Wu, and S. Li, Magnetic properties of Mn_3O_4 film with a coexistence of two preferential orientations, *J. Appl. Phys.* 116(2), 023906 (2014)
24. U. H. Pi, K. Won Kim, J. Y. Bae, S. C. Lee, Y. J. Cho, K. S. Kim, and S. Seo, Tilting of the spin orientation induced by Rashba effect in ferromagnetic metal layer, *Appl. Phys. Lett.* 97(16), 162507 (2010)
25. H. Y. Hwang, Y. Iwasa, M. Kawasaki, B. Keimer, N. Nagaosa, and Y. Tokura, Emergent phenomena at oxide interfaces, *Nat. Mater.* 11(2), 103 (2012)